Supplementary Material for

Pervasive ice sheet mass loss reflects competing ocean and atmosphere processes

Ben Smith*, Helen A. Fricker, Alex S. Gardner, Brooke Medley, Johan Nilsson, Fernando S. Paolo, Nicholas Holschuh, Susheel Adusumilli, Kelly Brunt, Bea Csatho, Kaitlin Harbeck, Thorsten Markus, Thomas Neumann, Matthew R. Siegfried, H. Jay Zwally

*Corresponding author. Email: besmith@uw.edu

This PDF file includes:

Materials and Methods
Supplementary Text
Figs. S1 to S8
Tables S1 and S2
References

Materials and Methods

The analysis presented here involves: (1) comparing surface height measurements from ICESat and ICESat-2; and (2) converting those measurements to ice-mass change by removing instrument biases, accounting for changes in ice-column density, and correcting for deformation of the solid Earth. The nature of the data and corrections applied are provided below.

Materials: Data from the ICESat laser altimeter mission

The ICESat mission (2003-2009) acquired data during 19 separate 8- to 37-day campaigns between February 2003 and October 2009 (45). The Geoscience Laser Altimeter System (GLAS) onboard ICESat had three redundant lasers, designated Laser 1, 2, and 3, with only one laser operating at a time (46). Due to faster than expected transmit pulse energy decline, Laser 1 failed after only 38 days of operations, completing a total of two campaigns (L1a, L1b) during February and March, 2003 (47). Laser 2 completed three 33- to 37-day campaigns (L2a, L2b, L2c; September 2003 to June 2004) before being turned off for transmit-energy considerations. Laser 3 completed 11 campaigns (L3a to L3k; October 2004 to October 2008) before it failed. Laser 2 was then turned back on for three final campaigns (L2d to L2f; November 2008 to November 2009) with the lowest transmit energy of the mission (mean transmit energy of 2.9-5.3 mJ/pulse for these campaigns, compared to 13.3-68.0 mJ/pulse for all other campaigns; (45)). Here we use only the high energy campaigns (Laser 2a to Laser 3k; 13 October 2003 to 19 October 2008).

Materials: Data from the ICESat-2 laser altimeter mission

NASA's Ice, Cloud and land Elevation Satellite-2 (ICESat-2)'s Advanced Topographic Laser Altimetry System (ATLAS) instrument is new technology for spaceborne measurement of surface height, vegetation and atmosphere. ATLAS emits short-duration (1.6 ns full width at half maximum), green (532 nm) laser pulses at a 10 kHz repetition rate and detects returns with a "photon-counting" system (48). ATLAS splits the transmit pulse using diffractive optics into six beams configured as three beam pairs, with spacing within and between pairs determined by spacecraft orientation (Figure S1). The times-of-flight for surface returns, combined with knowledge of the spacecraft position and orientation, provide estimates of the height of the surface beneath the satellite with 10 m horizontal accuracy and 0.03 m vertical precision (see calibration/validation discussion below). ATLAS's high precision, small footprint, multiple beams, and negligible penetration into the surface provides an unambiguous height measurement, allowing estimates of ice-sheet change, even in areas where cross-track slope ambiguity prevented robust interpretation of ICESat repeat-track data (24, 49). The slope-dependent performance of ICESat and ICESat-2 are presented in Figure S2.

In the years leading up to launch, the ICESat-2 Science Definition Team developed a set of processing techniques to obtain accurate surface-height measurements from ATLAS data for various applications (e.g., geolocated photon clouds (ATL03; (50)); land ice (ATL06; (51)); sea ice (ATL07; (52)); vegetation (ATL08; (53, 54))). These techniques take advantage of the large number of pulses that ATLAS emits every second by aggregating the height data for all photons returned from consecutive pulses, such that

surface height estimates are derived from collections of tens or hundreds of photons, as opposed to the approximately 3 to 12 photons returned from a single pulse. Following the ICESat-2 launch on 15 September 2018 there was a 120-day commissioning phase, followed by the public release of these data products to the broader scientific community in May 2019.

The ICESat-2 mission was designed to make repeat measurements over the ice sheets, revisiting its 1387 reference ground tracks every 91 days. Because of an on-board software problem during the commissioning phase, measurements during the first two cycles were displaced between one and four km from the reference tracks. This means that the 134 days of data used in this paper (October 14, 2018 - February 23, 2019) have smaller spacing between adjacent tracks than anticipated and allow comparisons with ICESat data at finer spatial resolution.

Methods: Data corrections and filtering
ICESat: We used ICESat data product GLA12 release 634 (55) with the "Guassian-centroid" (G-C) offset correction (56). Data were filtered using on-product variables, excluding data that did not meet the following criteria: "i_numPk == 1", "elev_use_flg == 0", "sigma_att_flg == 0" and "sat_corr_flg < 3". Finally, the following corrections and conversions were applied:

- Converted from Topex/Poseidon ellipsoidal heights to WGS84 ellipsoidal heights.
- Applied a saturation correction following (45).
- Applied an inter-laser bias correction: Subtracted 1.7 cm from Laser 2 and added 1.1 cm to Laser 3 (25).
- Corrected for ocean tide, load tide, and inverse barometer effects (IBE) over ice shelves (57–59)

ICESat-2: ICESat-2 ATL06 land ice data (60) are derived using a segmentation technique, where along-track geolocated photon data (ATL03) from each beam are divided into short (40 m) overlapping segments (51). For each segment, photon heights are fit as a function of along-track distance with a linear model. When both beams in a pair (offset by ~90 m across track) detect the surface, the cross-track surface slope is also estimated. Data are finally corrected for instrument specific biases (i.e., transmit-pulse shape and first-photon bias). Full details of the ATL06 algorithm are presented in (51). The final ATL06 product contains latitude, longitude, and height with respect to the WGS84 ellipsoid for each segment.

In this study, we used ICESat-2 data spanning the time period 2018-10-14 to 2019-02-23 (Release 001). Data were filtered three ways:
- Data flagged by the on-product ATL06 quality summary ("atl06_quality_summary") were removed.
- Data with high along-track height variability (adjacent segment height differences > 2 m) or containing fits to atmospheric scattering (surface heights > 10,000 m) were excluded.
- Crossover height differences within the ICESat-2 data were calculated, removing reference ground tracks (RGTs) associated with crossover errors > 1 m (likely driven by geolocation errors associated with orbit maneuvers).

Finally, the data collected over ice shelves were corrected for ocean tides, load tides, and inverse barometer effects (57–59).

Methods: dh/dt determination by crossover analysis

To generate surface height changes (dh/dt) from ICESat and ICESat-2, we performed a crossover analysis between ICESat and ICEsat-2, separating results for grounded and floating ice over Antarctica and Greenland. The result is a series collection of dh point measurements spanning ~10-16 years. For each orbital crossing between ICESat (single beam) and ICESat-2 (six beams) we obtain six crossovers. This is a substantial improvement in crossover-density (Fig. S3) compared with previous crossover analyses (61–63), allowing us to characterize small-scale features such as marginal ice streams and small ice shelves.

Local dh/dt outliers were identified by planar regression in 50km bins for Antarctic ice shelves and for Greenland, and in 20-km bins for Antarctic grounded ice. Values that fell outside of 10-sigma were excluded.

Methods: Correction for changes in accumulation and firn air content

To remove the height change signal associated with a change in column-averaged density, we must compute the change in the total firn air content (FAC) across both Greenland and Antarctica over the ICESat and ICESat-2 intervals. At this time, published firn densification model (FDM) simulations are not available through the ICESat-2 epoch (61, 64, 65); thus, we simulated the evolution of the firn column over the full time-period sampled by ICESat and ICESat-2 using the Community Firn Model (CFM) Version 1.0.3 (66).

The CFM was built off the Firn Model Intercomparison Experiment (FirnMICE (67)) and is open-source, modular in design, and presently contains modules that simulate the key physical processes that control the evolution of firn thickness and air content. The CFM uses a one-dimensional Langrangian grid; thus, each simulation is run independently of all others. The user is allowed to select from a variety of densification equations and parameterizations (64, 68–71). Heat transfer, grain growth, densification, and meltwater vertical transport (including percolation and refreezing) all depend on surface climate forcings: the CFM requires inputs of snow accumulation rate (snowfall-minus-sublimation), skin temperature, and surface meltwater to model these processes. A few different liquid water schemes are available within the CFM (72). Here, we implement a common bucket percolation scheme for efficiency; comparison with field data (72) did not indicate that using the more complex schemes would yield more accurate results, although the authors noted that a lack of field observations hindered their study from robustly quantifying differences between the different liquid water scheme model performance.

To reproduce FAC evolution using the CFM we must (a) generate surface climate forcings, (b) derive densification equation calibration coefficients, (c) implement simulations for both Greenland and Antarctica, which we describe below.

Climate Forcing: Changes in firn properties (e.g., thickness, FAC) through time are a function of anomalies in the long-term ambient climate. Thus, firn densification models

require a reference climatology that is long enough to capture the appropriate climatological mean. On ice sheets, surface processes operate at length scales shorter than can currently be resolved by global atmospheric models (7), and as a result, regional climate models (RCMs) are the preferred (1, 2, 8). The improved spatial resolution and more advanced surface- and near-surface physics of RCMs come at a significant time cost, however, limiting our ability to achieve rapid, up-to-date products. Our approach employs a compromise that provides high resolution output at lower computation cost, in which we hybridize NASA's global Modern-Era Retrospective analysis for Research and Applications, Version 2 (MERRA-2) with an offline high-resolution MERRA-2 'replay,' (described in detail below).

MERRA-2 is an atmospheric reanalysis developed at the Global Modelling and Assimilation Office (GMAO) at NASA Goddard Space Flight Center (73). By assimilating satellite, airborne, and ground observations, MERRA-2 provides global atmospheric variables spanning the modern satellite era (1980 through present) at a relatively short release latency (sub-monthly). Here, we simulate FAC from hourly snowfall, evaporation (which includes sublimation), and skin temperature fields from January 1, 1980, through March 31, 2019, provided at 0.625° longitude x 0.5° latitude resolution. Studies indicate that MERRA-2 provides the most realistic snow accumulation rates and temperatures over Antarctica, compared to other reanalyses (74, 75). Where higher resolution is required (i.e., in the presence of steeply sloping surface topography), we derive a hybrid, 12.5 km resolution product, referred to as 'MERRA-2 Hybrid', using an offline 'replay' run of MERRA-2, referred to as 'M2R12K'.

The M2R12K run only spans a 15-year interval (2000-2014), but was run at 12.5 km resolution over both Antarctica and Greenland, comparable to RCMs for Greenland (29, 76) and more refined than RCMs for Antarctica (77, 78). To generate the MERRA-2 Hybrid, we remove the seasonal cycle in MERRA-2 hourly accumulation and skin temperature by removing monthly means, interpolate the residual to the M2R12K 12.5 km grid, and then combine it with the seasonal signal from the M2R12K. In such a manner, we preserve the high-resolution magnitudes and seasonal variations from the M2R12K while adding on the higher-frequency variability from MERRA-2. The final MERRA-2 Hybrid product is a 12.5 km, hourly representation of the surface climate for both the Greenland and Antarctic ice sheets spanning nearly four decades (January 1, 1980 - March 31, 2019).

While melt processes are included in MERRA-2, only surface runoff was retained as an output variable. Thus, we develop a simple surface meltwater model to use as CFM forcing. For both ice sheets, we use a degree-day method approach (79) to estimate meltwater fluxes (ΣM):

$$\Sigma M \ = \ DDF * \Sigma \ (T_{skin} - T_0)\Delta t; \ T_{skin} > T_0. \tag{1}$$

The degree-day factor (DDF) is a calibrated value (units: kg m^{-2} per degree day) that relates accumulated hourly skin temperature (T_{skin}) above a given threshold temperature (T_0) to total meltwater flux over a given time interval (Δt = 1 hour). For Antarctica, annual surface meltwater fluxes spanning 1999 to 2009 from (80), interpolated to our 12.5 km MERRA-2 Hybrid grid, provide the basis of our degree-day factor calibration. We also evaluate the model's ability to reproduce Antarctic-wide annual melt rates by calibrating the model to a range of threshold temperatures (265 K - 273 K). For each threshold scenario, the degree-day model is calibrated on a cell-by-cell

basis by relating the accumulated hourly temperatures above that given threshold over an entire year and the annual meltwater flux at that grid cell from (80). Linear regression of these variables provides calibrated DDF for each grid cell and each temperature threshold. We determine the optimal temperature threshold by assessing how well the Antarctic-wide annual meltwater flux from our degree-day model matches that from (80). For Antarctica, we use $T_0 = 269.35$ K. Hourly melt values are then calculated using $T_0 = 269.35$ K and the DDFs calibrated to that temperature threshold.

Greenland hourly meltwater fluxes are estimated using the same approach; however, no observations of surface meltwater fluxes comparable to (80) exist for Greenland. Thus, we calibrate the model to annual meltwater fluxes from the MARv3.5.2 RCM (29) covering 1980 through 2014. By calibrating to annual fluxes, we allow the MERRA-2 Hybrid climate to control the variability in melt, while largely retaining the overall magnitude of fluxes from MAR. For Greenland, we find that $T_0 = 270.00$ K best replicates Greenland meltwater fluxes from MAR.

Whereas the aforementioned variables are all generated at hourly resolution, to maintain computation efficiency, we develop five-, ten-, and twenty-day resolution MERRA-2 Hybrid products that provide forcings for CFM simulations. For the flux variables (accumulation and melt), the hourly values are integrated over the desired time window. Because firn densification is non-linearly dependent on skin temperature, we create effective skin temperatures for each desired time window to capture the effects of strong diurnal variability. We do this by calculating the hourly densification rate constant (c) using an Arrhenius type sensitivity to temperature ($c = e^{\frac{-E}{RT}}$) where E is the activation energy, R is the gas constant, and T is the skin temperature. We next take the mean of the hourly rate constants over each time window of interest, and then invert the Arrhenius equation to recover the effective skin temperature. The result is a temperature product that reproduces the mean densification rates over our target window. The activation energy used is selected from a calibration process, described below.

Calibration: We calibrated the densification equations in the CFM using a database of 256 published depth-density measurements from both Greenland (72) and Antarctica (184); thus, the calibration is applicable to both ice sheets. We used the Arthern et al. (71) densification equation as the basis of our simulations, and we used the calibration database to modify its parameterization. Specifically, the rate of densification is separated into two stages:

$$\frac{d\rho}{dt} = c_0(\rho_i - \rho); \ \rho \leq 550 \ kg \ m^{-3}, \tag{2}$$
$$\frac{d\rho}{dt} = c_1(\rho_i - \rho); \ \rho > 550 \ kg \ m^{-3}. \tag{3}$$

The densification rate constants depend on the total mass above a given firn parcel (here, represented as the mean accumulation rate, $\underline{b}$, experienced since that parcel was deposited), the temperature of the parcel, T, and the mean annual temperature, T_{avg}:

$$c_0 = 0.07 \ \underline{b}^{\alpha_0} \ g \ exp(-E_c/RT + -E_g/RT_{avg}), \tag{4}$$
$$c_1 = 0.03 \ \underline{b}^{\alpha_1} \ g \ exp(-E_c/RT + -E_g/RT_{avg}), \tag{5}$$

6

where g is the gravitational acceleration constant, E_c is the activation energy for lattice diffusion (60 kJ mol⁻¹), E_g is the activation energy for grain growth (42.4 kJ mol⁻¹), the constants are empirically derived, and $\alpha_0 = \alpha_1 = 1$ (*71*). Results from (*64*) indicated that these densification equations resulted in rates that were too rapid, so the model was calibrated using measured depth-density profiles. The authors calibrate the FDM by relating the ratio of the observed to modeled depth of critical densities (i.e. 550 kg m⁻³ and 830 kg m⁻³) to the mean annual accumulation rate. Here, we elected to maintain the original form of the equations 4-5 by modifying the relationship between the densification rates and overburden (α) and temperature (E_c).

The calibration procedure was iterative, as the climate forcing (the effective skin temperature) is dependent on the activation energy, E_c. We simulate 226 firn depth-density profiles with the initial configuration of $\alpha_0 = \alpha_1 = 1$ and $E_c = 60$ kJ mol⁻¹. The number of simulations is less than the actual number of observations (256) as some fall within the same 12.5 km grid cell. For each of the simulations, the model spin-up involved repeating the 39-year modern climate (1980-2019) for as many years as it takes to refresh the firn column to a density of 900 kg m⁻³. The slope of the density profile with depth is approximately linear when taking its logarithm (i.e., $ln(\frac{\rho}{917-\rho})$; (*68*)), so we calculated the slope of the logarithmic density versus depth for the two stages of densification and compared it to the equivalent model output using the Arthern et al. configuration (*71*). The ratio of the observed slopes (*R*) to the modeled slopes provided the necessary correction (or calibration coefficient) for each site; however, in order to calibrate the model, we must relate these calibration factors to the climate forcing. Fitting our calibration procedure to the original model form, the correction term takes the form:

$$R_0 = \underline{b}^{\beta_0} exp(\frac{-E_0}{RT}), \tag{6}$$
$$R_1 = \underline{b}^{\beta_1} exp(\frac{-E_1}{RT}). \tag{7}$$

These set of equations are linearized (intercept forced to zero) to allow us to solve for the β_0, β_1 and E_0, E_1 using the ratios R:

$$ln(R_0) = \beta_0 \; ln(\underline{b}) - E_0 \frac{1}{RT}, \tag{8}$$
$$ln(R_1) = \beta_1 \; ln(\underline{b}) - E_1 \frac{1}{RT}. \tag{9}$$

For the calibration, we calculated $\underline{b}$ for both stages of densification as the mean overburden, expressed as the mean accumulation rate experienced, within the representative stage. Temperature T is the mean effective temperature at that site for stage 1, and the mean temperature of the firn column for densities higher than 550 kg m⁻³. Since T is dependent on the activation energy, which is modified through our calibration procedure, we iterated the calibration process, each time updating the activation energy and our calculation of effective temperature, until convergence of the calibration parameters.

The calibration coefficients converge to the following:

$$\beta_0 = -0.1483, \beta_1 = -0.3510, E_0 = -731\, J\, mol^{-1}, E_1 = -2861\, J\, mol^{-1}.$$
(10)

These required a single iteration for stage 1 and two iterations for stage 2. The new coefficients resulted in more rapid densification rates under lower accumulation rates and less rapid under higher accumulation rates for both stages, although the impact is stronger in the second stage. Similarly, densification rates are reduced with increasing temperature, especially in the second stage. For the first stage, the mean absolute error in modeled depth-density slope is reduced from 55% of the mean slope when using the original Arthern et al. parameterization (*71*) to 19% when using our calibrated model. For the second stage, the improvement in mean absolute error is similar, reduced to 12% from 55%.

Greenland GSFC-FDM v0 Simulations. The reference climate interval for the Greenland simulations is 1980-1995, ending prior to the onset of extreme melt years. Thus, the spin up for all the simulations involved repeating the 1980-1995 climate until the firn column was refreshed to a depth where dry snow density equals 900 kg m^{-3}. Following spin up, the FDM runs over the full 1980-2019 interval. Approximately 10,900 of the MERRA-2 Hybrid 12.5 km grid cells fell within our grounded ice sheet mask (*81*); however, we eliminated ~1,300 from the FDM simulations where the mean sublimation rates comprised 2/3rds of mean snowfall rates or where the mean of the combined mass loss fluxes (melt and sublimation rates) was larger than mean snowfall rate. In total, we ran 9,600 GSFC-FDM simulations across the Greenland Ice Sheet at five-daily resolution, spanning the full 1980-2019 interval. Applied firn correction is shown in Figure S4.

Antarctic GSFC-FDM v0 Simulations. The reference climate interval for the Antarctic simulations is 1980-2019 (i.e., the full MERRA-2 Hybrid interval). Similar to the Greenland simulations, spin up involved refreshing the firn column to a depth where dry snow density equals 900 kg m^{-3} but differs in that the 1980-2019 climate is instead repeated. Following spin up, the FDM runs over the full 1980-2019 interval. Approximately 87,200 of the MERRA-2 Hybrid 12.5 km grid cells fell within our grounded and floating ice sheet mask (*81*), but to make the simulations more computationally efficient, we ran the GSFC-FDM at a subset of the total number. This is justified by the fact that the spatial scales of the MERRA-2 Hybrid climate are quite large, especially over the relatively flat plateau. Specifically, we grouped cells together if neighboring cells differ by the following thresholds: mean annual temperature less than 0.75 K, the root mean square deviation (RMSD) of net accumulation (P-E) is less than 10% of the mean annual P-E, the RMSD of skin temperature is less than 0.25 K, and the RMSD of melt (if any) is less than 0.05 m i.e. yr^{-1}. This subsetting eliminated near-redundant simulations, saving simulation time and reducing the total simulations by more than half (~38,000). It is important to note, that this effort only eliminated simulations where local climate differences are very small (i.e., the dry plateau); however, in places of strong gradients (e.g., the Antarctic Peninsula, the Transantarctic Mountains, coastal escarpment areas, ice shelves), few (if any) were removed, maintaining the gradients present within the 12.5 km MERRA-2 Hybrid. As done with the Greenland simulations, we eliminated ~1,900 (of the original 87,200) of the simulations where the mean

sublimation rate comprised 2/3rds of mean snowfall rate or where the mean of the combined mass loss fluxes (melt and sublimation rates) was larger than mean snowfall rate.

We further improve efficiency by varying the temporal resolution of the simulations. Using the 226 calibration simulations (run at five-, ten-, and twenty-daily resolution), we evaluated the differences in the trend in FAC for different time resolutions for every 13-year interval (equivalent to the ICESat/ICESat-2 interval) over the full 1980-2019 time series. Specifically, we estimated the 95% bounds in the difference between the five-daily and the ten- and twenty-daily simulations at each site. We fit a linear model to these bounds using the mean annual snow accumulation and skin temperature as the predictors. The model was then applied to all of Antarctica to approximate the error in FAC trends that result from a reduction in the temporal resolution. We aimed to have a similar accuracy in FAC change as the measured height change; thus, we assume an error threshold of 0.4 cm yr^{-1} (ICESat-2 Science Requirement; (*48*)). All cells where the modeled ten- or twenty-daily error was less than 0.4 cm yr^{-1} were run at ten- or twenty-daily, respectively. The remainder were run at five-daily resolution. The result is near concentric rings centered over the plateau of twenty-daily simulations surrounded by a narrow ring of ten-daily, ending with a wide band 5-daily around the periphery. All simulations were interpolated to five-daily resolution.

In total, we ran 37,700 GSFC-FDM simulations across the Antarctica Ice Sheet and the peripheral ice shelves and islands, spanning the full 1980-2019 interval. This subset is then interpolated to the full 12.5 km grid. Applied firn correction is shown in Figure S5.

Uncertainty in FAC Trends (εFAC). Due to a lack of constraint on the uncertainties in the parameterizations of firn evolution within the CFM as well as in the atmospheric forcing, we estimate the uncertainty in ~12.5 year trends (ICESat - ICESat-2 interval) in FAC by comparison with IMAU-FDM (*63, 82-83*). The IMAU-FDM simulation end prior to the ICESat-2 epoch; thus, the model intercomparison covers their contemporaneous time interval (January 1980 - December 2016). Our approach is identical for both Greenland and Antarctica.

The IMAU-FDM FAC is first interpolated to our 5-km grid (see Gridding section) and the GSFC-FDM 5-daily time steps. Because deviations to the long-term mean drive firn height changes, we next remove the 1980-2016 mean FAC from each grid cell. Rather than solely look at the differences in dFAC/dt over our time window of interest, we use information from the entire time series to derive uncertainties. Specifically, we replicate our FAC change estimates at a time scale comparable to that used in the ICESat-ICESat-2 comparison by calculating dFAC/dt estimates over a running 12.5-year window beginning January 1980 for both the GSFC and IMAU-FDMs. For each 12.5 year window, we calculate the difference in dFAC/dt between the two models, and we assign an uncertainty in dFAC/dt to that grid cell that is equal to the standard deviation of the 12.5-year running differences (at five-daily resolution, n = 1582). This defines the spatially varying uncertainties to the GSFC-FDM FAC trends that reflect the differences in FDM simulations.

Because atmospheric processes over the ice sheets are typically correlated over long length scales, we account for their spatial correlation when propagating uncertainty into basin-wide FAC change estimates. For each basin (Figure S5), we generate a correlation matrix based on the time series of differences in dFAC/dt between IMAU-FDM and

GSFC-FDM. If the uncertainties between grid cells within a basin are completely independent, the correlation will be zero and the combined uncertainty is simply the square root of the sum of squares. If the correlation is greater than zero, the uncertainties are spatially correlated, and their combined uncertainty will be larger than the value calculated assuming pure independence. If the correlation is less than zero, the uncertainties always act opposite one another, and their combined uncertainty will be less than the value calculated assuming pure independence as their errors offset. Once errors for each basin have been appropriately propagated, we assume that basin errors are largely independent of one another and simply apply the square root of the sum of squares to obtain ice-sheet-wide errors. Analysis of climate-model output (*84*) suggests that atmospheric conditions within basins are often locally correlated as well as distally anti-correlated. Therefore, at the ice-sheet scale, errors will be amplified and dampened by a range of heterogeneous atmospheric patterns. Further experiments propagating errors over aggregated basins suggests that errors remain of a similar magnitude but can be larger or smaller than assuming basin independence, so we argue that our approach provides a robust error estimate at the ice-sheet-scale.

Methods: Solid Earth corrections

We estimated changes in vertical surface displacement due to Glacial Isostatic Adjustment (or post-Glacial Rebound), the long-term viscoelastic response of the Earth to changes in ice load since the Last Glacial Maximum (LGM). Uncertainties in global ice history and the Earth's internal rheological structure lead to uncertainties in modern-day vertical displacement. To account for this deformation, we calculated the mean rate of vertical displacement using coefficients from three published estimates (*85–88*) for Antarctica and two estimates (*88*, *89*) for Greenland. All fields were truncated to spherical harmonic degree and order 120 for consistency and converted to vertical motion, following (*90*). For Antarctica, uncertainty due to GIA was estimated as the standard deviation between the three fields; for Greenland, uncertainties were estimated as the absolute value of the difference between the two fields. GIA corrections applied to our Greenland and Antarctic solutions are shown in Figures S4 and S5, respectively.

More recent changes in ice sheet mass can induce an elastic response of the solid Earth with measurable crustal displacements (*91*). To estimate this component, we first computed surface displacements due to a 1 m change in solid ice over a 5 km grid cell using LoadDef (*92*), assuming a spherically symmetric Earth with a density structure from PREM (*93*). We then used this to generate a matrix G that related mass change in each grid cell (m) to the corresponding vertical displacements (d) across the grounded ice sheet through $d = Gm$. We propagated uncertainties in m into uncertainties in d; this estimate relies on the assumption that the errors in our knowledge of the density structure of the solid earth and that the relationship between changes in surface mass loading and corresponding vertical displacements were negligible. Elastic corrections applied to our Greenland and Antarctic solutions are shown in Figures S4 and S5, respectively.

Methods: Correction for changing ice shelf area

Surface height change measurements (*dh/dt*) taken over floating ice shelves represent changes in freeboard, not changes in thickness (as in the grounded ice), thus delineating between grounded and floating areas is critical for mass change calculations.

Ice shelf area increases continuously due to advection and reduces only episodically due to calving, with reduction time-scales dependent on the length of the calving cycle (*94*, *95*). We derived a conservative ice shelf mask using the intersection of ice shelf polygons from (*96*) and (*5*), and hand-drew a new ice-shelf mask to account for the calving of the Western edge of the Thwaites ice shelf. For the Larsen C Ice Shelf, we included a new ice boundary to account for calving of iceberg A-68 in July 2017 (*97*). To avoid including elevation changes associated with ice-front motion or rift propagation, we removed all crossovers in which at least one elevation measurement fell within 5 m of mean sea level, as well as all floating-ice crossovers whose elevation change reflected a mean rate of change greater than 2 m yr^{-1} (equivalent to ~30 m of surface elevation change or ~300 m of thickness change between the two missions).

Methods: Gridding

Height-change measurements were interpolated onto a 5 km by 5 km grid, using a distance-weighted gaussian kernel. The kernel had a correlation length of 10 and 20 km for Antarctica and Greenland respectively, incorporating the 200-nearest observations (up to 25 km away from the kernel center). Finally, we apply a 3x3 median filter to all regions, except to floating ice, to remove or reduce artifacts in in the gridded dh/dt values. Corrections required to convert dh/dt to mass were interpolated to the observation points, and the resulting dm/dt values were then gridded using the same algorithm

Methods: Uncertainty estimation

Our analysis contains several sources of uncertainty in both the height change estimation and the corrections that are applied to convert between volume/freeboard change to mass change. Details on the assumptions used to derive individual sources of uncertainty can be found in Sections 2.1 through 2.5. Sources of uncertainty are separated into those assumed to be fully correlated on continental or basin scales and those that we expect to be uncorrelated at spatial scales greater than 25 km^2.

We refer to the error that is uncorrelated at spatial scales greater than 25 km^2 as the random error (εr). εr is composed of errors originating from instrument precision, ground finding blunders (e.g. low-lying cloud and blowing snow), imprecise tidal corrections over floating ice, and interpolation errors. We approximate εr as the standard deviation of dh/dt values within each 5 km by 5 km grid cell (Figure S6). This is likely a conservative estimate, as the mean of the dh/dt values should exhibit a central tendency (meaning that the error in the mean is likely smaller than the standard deviation). εr is added in quadrature for each 5 km by 5 km grid cell, and becomes negligible when integrated over large spatial scales.

Correlated errors arise from biases in the altimetric measurements (εA), biases in firn air content trends (εFAC), error in the Glacial Isostatic Adjustment (εGIA), and errors in the computed elastic response of the solid earth to changes in overburden (εE). εA, εGIA, and εE are assumed to be correlated at continental scales. We do not account for uncertainties arising from seasonal aliasing (differences in time of year between height measurements. Given the long interval between ICESat and ICESat-2 measurements (2003-2009 to 2018-2019), seasonal aliasing has minimal impact on our solution.

Supplementary Text

ICESat-2 vertical accuracy and precision

The vertical accuracy and precision of the ATL06 (Release 001) data product were assessed using ground-based kinematic GPS data from a region referred to as the 88S Traverse (*98, 99*). The ~750 km traverse route, based out of South Pole Station, includes ~300 km along the ICESat-2 ground-track convergence zone at 88º S latitude. The ground-based kinematic GPS data were post-processed using Precise Point Positioning (PPP) methods (*100*) in a commercial software package (Inertial Explorer) and have an uncertainty of 5.3 cm. Further details of ground-based assessment are in (*99*).

Direct comparisons were made between the 88S Traverse GPS surface heights and the ATL06 surface heights (assuming no change in the surface between the traverse epoch and ICESat-2 overflight) to determine the ATL06 bias and precision, reported as bias ± the 1σ surface-measurement precision. The data assessed spanned from 14 October, 2018 to 1 May 2019 (Figure S7). For all six beams, the bias was less than 3 cm and the surface measurement precision were less than 9 cm. For the center, strong beam, the bias was +1.7 cm (the ATL06 surface is slightly higher than the surface based on the ground-based GPS data) with a 7.7 cm 1-sigma standard deviation, which is taken to be the per-measurement precision ((*99*) Table 1). Further details of the ATL06 assessment are in (*99*).

Borsa et al (*25*) report an overall ICESat (Release 634) bias and surface measurement precision of 0.0 ± 4.0 cm. Thus, based on the 88S Traverse assessment, the first 6 months of ICESat-2 ATL06 data are comparable to ICESat data with respect to surface height accuracy.

dm/dt by drainage basin

Ice-sheet scale mass change is presented in Table 1. Those results are broken down by drainage basins (Figure S8) in Tables S1 and S2.
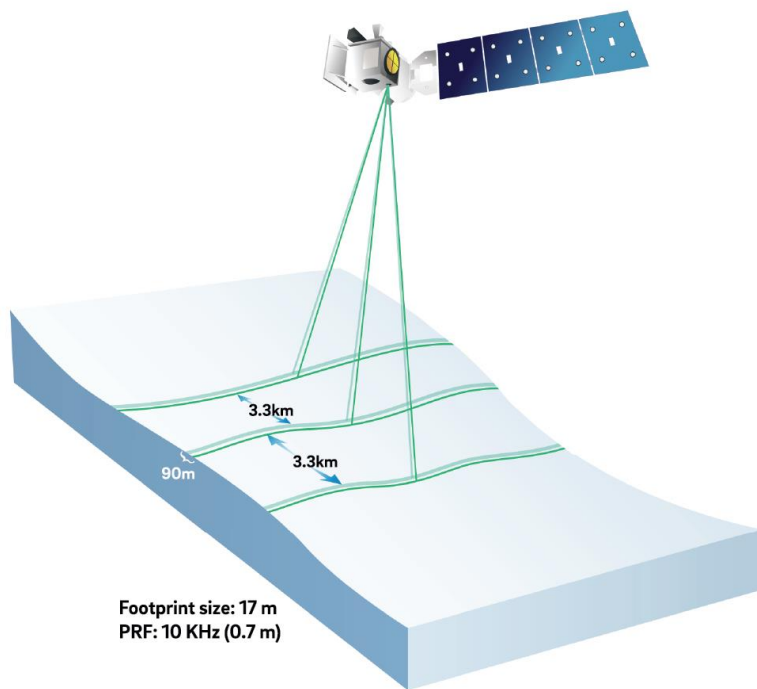
Fig. S1.

Schematic of ICESat-2's ATLAS laser altimeter showing the split-beam pattern. ATLAS is a "photon-counting" instrument, i.e. it emits a series of green laser pulses that are received and counted by a single-photon detectors. The transmit pulse is divided into three "beam pairs", with 3.3 km between each pair. Each beam pair has a "weak" beam and a "strong" beam (where strong is defined as approximately four times brighter than weak); this is designed to provide the necessary dynamic range to capture enough return photons from both bright (ice) and dark (ocean) surfaces. Reproduced and modified from (*51*).

The plot shows Standard Deviation (cm) on the y-axis versus Slope (deg) on the x-axis, with the following legend:

- GT1L: $\sigma_p = 09, \sigma_0 = 0.06$ (m)
- GT1R: $\sigma_p = 06, \sigma_0 = 0.05$ (m)
- GT2L: $\sigma_p = 08, \sigma_0 = 0.05$ (m)
- GT2R: $\sigma_p = 07, \sigma_0 = 0.05$ (m)
- GT3L: $\sigma_p = 07, \sigma_0 = 0.05$ (m)
- GT3R: $\sigma_p = 10, \sigma_0 = 0.06$ (m)
- ICE-1: $\sigma_p = 18, \sigma_0 = 0.09$ (m)

$$\sigma_i^2 = \sigma_0^2 + \sigma_p^2 \cdot \alpha^2$$
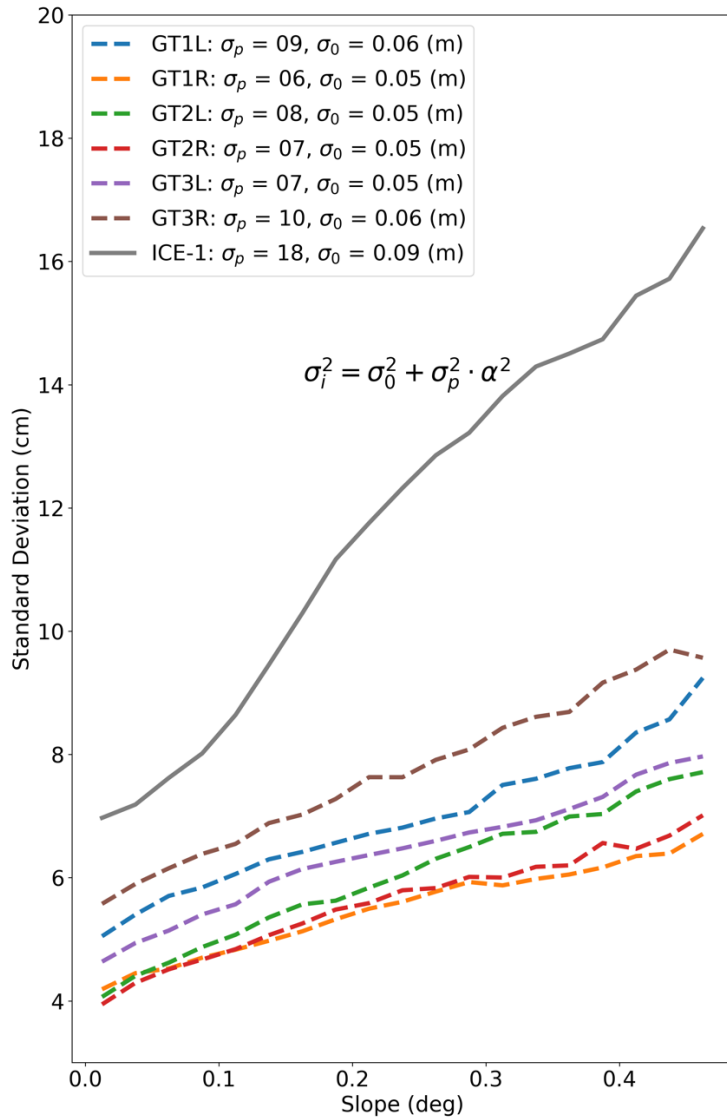
Fig. S2

Standard deviation from intra-ICESat (solid) and intra-beam ICESat-2 (dashed, release 2) crossovers with a time span less than 30-days, as a function of surface slope. ICESat-2 performs comparably over a range of cross track slopes, while ICESat cross-over errors are higher at all slopes, increasing by a factor of 2.5 over the range of slopes sampled. The values in the legend represent the estimated geolocation error (σ_p) and noise-floor (σ_0), calculated by fitting an error model to the data.
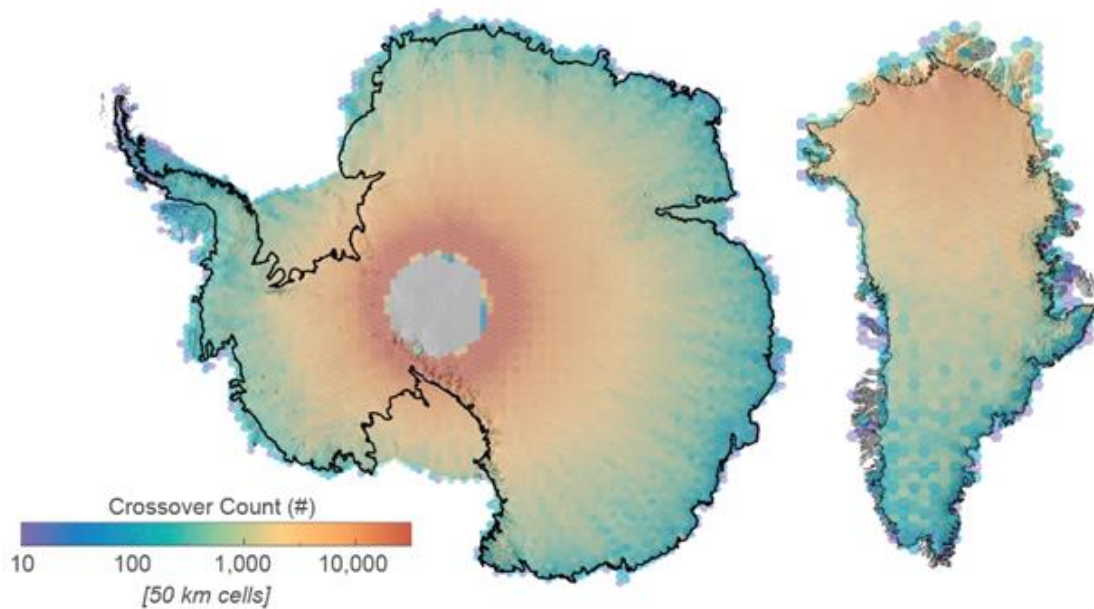
Fig. S3

Spatial coverage of ICESat (2003-2009) to ICESat-2 (2018-2019) crossovers, providing near-complete coverage of Greenland and Antarctica to 86°S, including the margins with steep slopes, the interior, and the ice shelves. This detailed sampling allows for the most complete assessment of total ice sheet mass change to date.
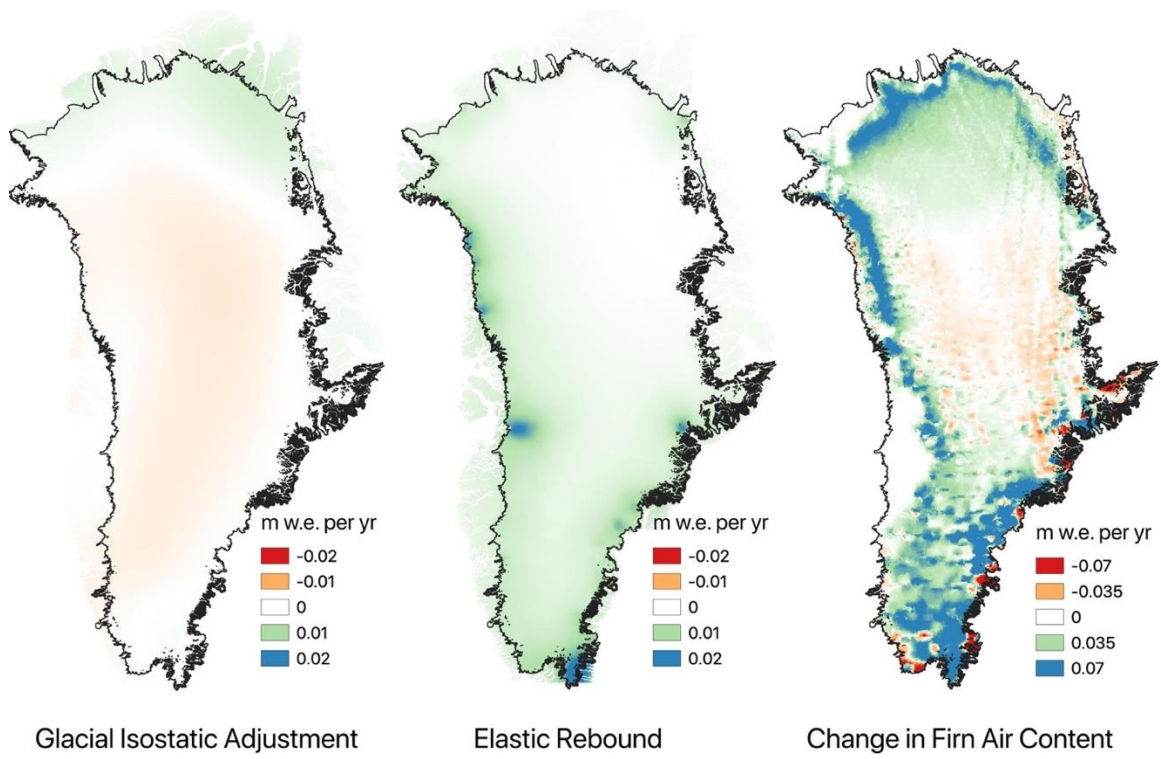
Fig. S4
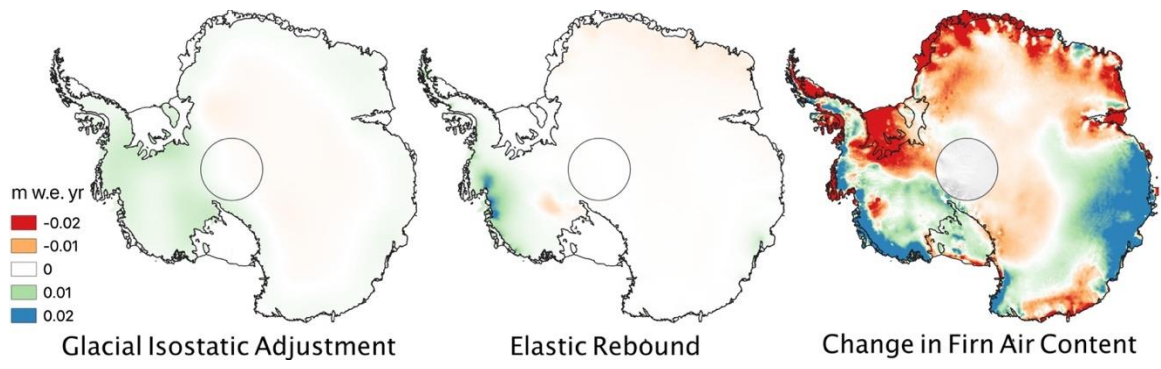Corrections applied to convert Greenland elevation changes to mass changes.

m w.e. yr
-0.02
-0.01
0
0.01
0.02

Glacial Isostatic Adjustment   Elastic Rebound   Change in Firn Air Content

Fig. S5.
Corrections applied to convert Antarctic elevation changes to mass changes.
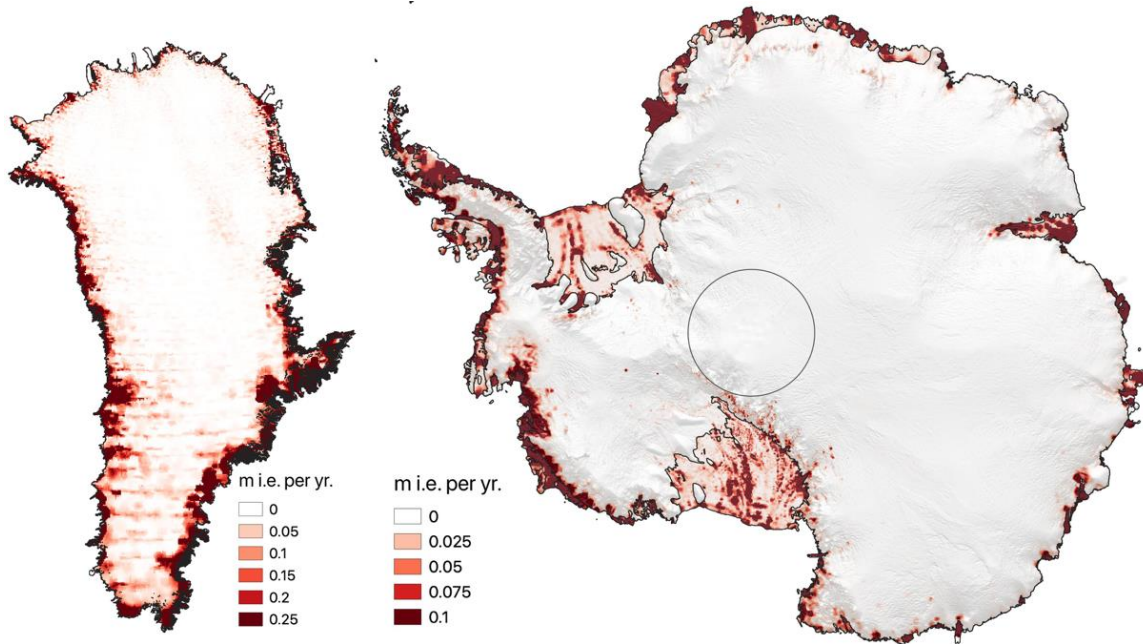
Fig. S6.
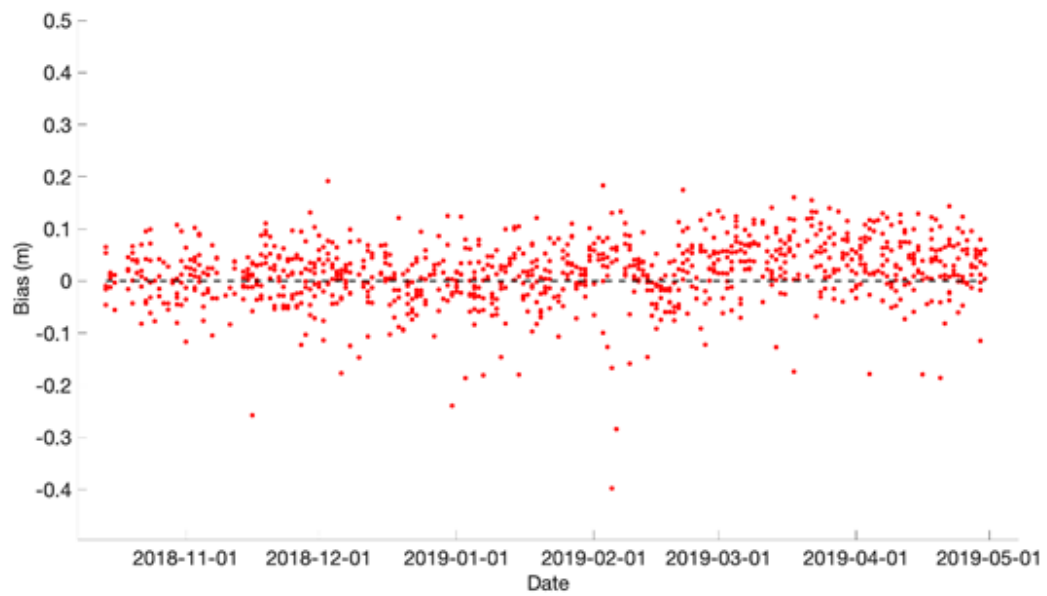RMS error of elevation change rates within each 5 km by 5 km solution grid.

Fig. S7.

ATL06 surface height bias (in m, for the center strong beam) relative to the 88S Traverse surface heights derived from GPS data.
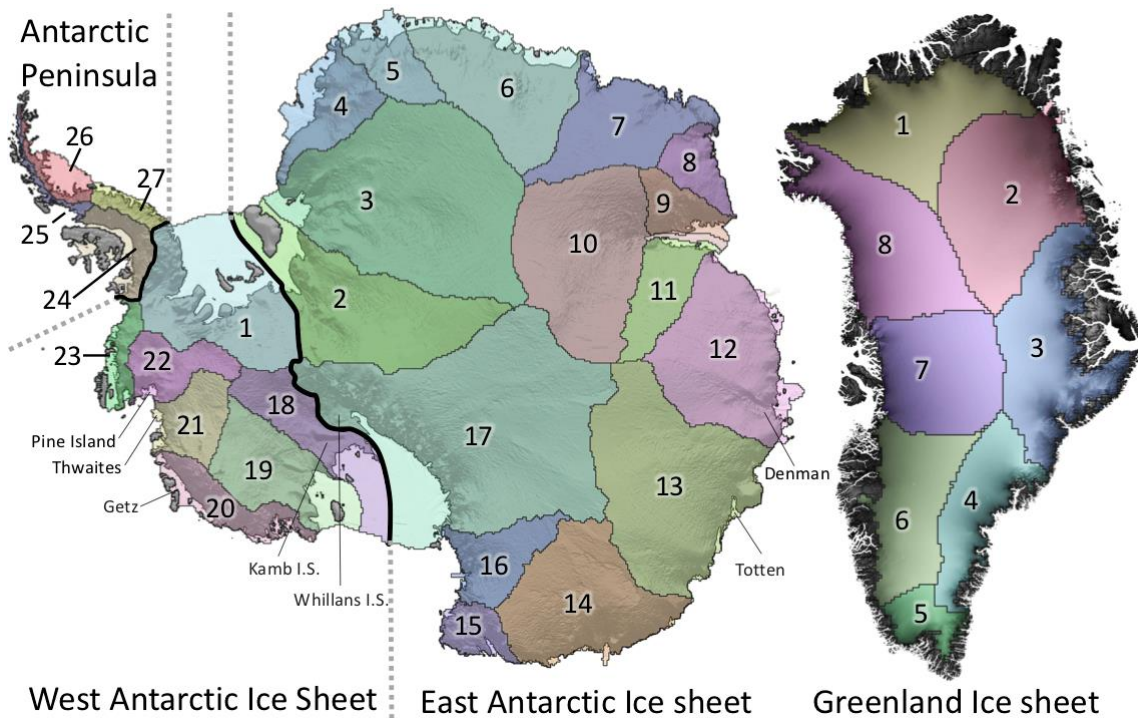
Fig. S8.

Map of drainage basins for Antarctica and Greenland. Antarctic subdivisions of the Antarctic Peninsula (AP: 24-27), West Antarctic Ice Sheet (WAIS: 2-17) and the East Antarctic Ice Sheet (EAIS: 1, 18-22, 23) are delineated with heavy black lines.

Table S1.

Volume and mass change of Antarctic grounded and floating ice by drainage basin including Firn Air Content (FAC), Elastic and Glacier Isostatic Adjustment (GIA) corrections.

Basin	Grounded Ice dV/dt (km³/y)	dFAC/dt (km³/y)	Elastic uplift (km³/y)	GIA (km³/y)	Mass change (Gt/y)	Ice Shelves dV/dt (km³/y)	dFAC/dt (km³/y)	Mass change (Gt/y)
1	23.3 ± 1.1	5.6 ± 6.9	0.7 ± 0.1	3.9 ± 0.0	12 ± 6	5.2 ± 0.6	6.4 ± 4.8	-15.2 ± 45
2	4.9 ± 1.2	1.2 ± 2.5	0.2 ± 0.1	1.3 ± 0.0	2 ± 3	1.7 ± 0.4	0.5 ± 1.1	9.8 ± 10
3	23.8 ± 1.5	6.4 ± 3.3	-0.5 ± 0.1	-0.6 ± 0.0	17 ± 3	1.8 ± 0.2	0.2 ± 0.2	13.5 ± 3
4	12.3 ± 0.7	3.4 ± 2.3	-0.2 ± 0.1	0.4 ± 0.0	8 ± 2	3.5 ± 0.3	2.7 ± 1.4	5.2 ± 13
5	12.6 ± 0.6	4.0 ± 2.0	-0.2 ± 0.0	0.2 ± 0.0	8 ± 2	2.6 ± 0.3	2.8 ± 0.6	-3.6 ± 6
6	28.6 ± 1.0	6.0 ± 5.2	-0.7 ± 0.1	0.4 ± 0.0	21 ± 5	4.5 ± 0.3	3.6 ± 1.5	4.4 ± 14
7	30.6 ± 0.8	3.4 ± 6.1	-0.6 ± 0.1	0.6 ± 0.0	25 ± 6	0.6 ± 0.1	0.0 ± 0.2	5.2 ± 2
8	10.2 ± 0.5	2.5 ± 1.1	-0.2 ± 0.0	0.2 ± 0.0	7 ± 1	0.0 ± 0.0	0.0 ± 0.0	-0.4 ± 1
9	1.7 ± 0.5	0.4 ± 1.9	-0.1 ± 0.0	0.2 ± 0.0	1 ± 2	1.2 ± 0.2	1.2 ± 0.9	-0.2 ± 9
10	6.4 ± 1.2	1.5 ± 2.8	-0.3 ± 0.1	-0.2 ± 0.0	5 ± 3	1.7 ± 0.2	0.9 ± 0.5	6.2 ± 5
11	1.7 ± 0.6	0.6 ± 1.5	0.0 ± 0.0	0.1 ± 0.0	1 ± 2	0.7 ± 0.1	0.3 ± 0.1	3.1 ± 2
12	-11.6 ± 1.0	-14.2 ± 5.4	0.0 ± 0.1	0.4 ± 0.0	2 ± 5	0.0 ± 0.2	0.1 ± 0.7	-1.0 ± 7
13	-35.2 ± 1.2	-14.5 ± 15.1	0.5 ± 0.1	0.6 ± 0.0	-20 ± 14	0.0 ± 0.1	-0.2 ± 0.6	1.2 ± 6
14	5.6 ± 1.0	2.0 ± 9.5	0.0 ± 0.1	0.3 ± 0.0	3 ± 9	0.8 ± 0.1	0.2 ± 0.5	4.5 ± 5
15	-4.0 ± 0.4	-2.0 ± 2.2	0.1 ± 0.0	0.1 ± 0.0	-2 ± 2	-0.3 ± 0.1	-0.1 ± 0.2	-2.1 ± 2
16	2.5 ± 0.6	-0.8 ± 2.6	0.0 ± 0.0	0.1 ± 0.0	3 ± 2	-0.1 ± 0.1	0.1 ± 0.1	-1.6 ± 1
17	13.1 ± 1.7	3.0 ± 6.9	0.1 ± 0.1	1.4 ± 0.0	8 ± 7	6.8 ± 0.6	-0.4 ± 1.0	61.4 ± 10
18	25.3 ± 0.8	-1.6 ± 2.5	-0.1 ± 0.1	1.9 ± 0.0	23 ± 2	1.7 ± 0.4	-0.7 ± 0.4	21.0 ± 5
19	-4.3 ± 0.8	-2.2 ± 2.0	0.6 ± 0.1	1.6 ± 0.0	-4 ± 2	2.3 ± 0.4	0.1 ± 0.8	19.0 ± 8
20	-53.7 ± 0.6	-7.5 ± 3.6	1.2 ± 0.1	0.5 ± 0.0	-44 ± 3	-6.8 ± 0.3	-1.0 ± 1.0	-48.8 ± 10
21	-88.2 ± 0.6	-0.3 ± 4.5	1.9 ± 0.1	0.7 ± 0.0	-83 ± 4	-4.0 ± 0.1	0.0 ± 1.0	-33.6 ± 9
22	-67.4 ± 0.6	-1.2 ± 3.5	1.6 ± 0.1	0.9 ± 0.0	-63 ± 3	-1.0 ± 0.1	0.2 ± 0.2	-10.1 ± 2
23	-10.7 ± 0.4	-0.7 ± 2.9	0.5 ± 0.0	0.5 ± 0.0	-10 ± 3	0.5 ± 0.2	1.3 ± 0.9	-8.3 ± 8
24	-13.7 ± 0.5	0.5 ± 3.2	0.4 ± 0.1	0.6 ± 0.0	-14 ± 3	-1.0 ± 0.2	1.4 ± 1.9	-22.1 ± 18
25	-10.9 ± 0.2	-0.1 ± 2.5	0.1 ± 0.0	0.1 ± 0.0	-10 ± 2	0.0 ± 0.0	0.0 ± 0.0	0.0 ± 0
26	-16.1 ± 2.3	0.9 ± 1.8	0.2 ± 1.7	0.2 ± 2.2	-16 ± 3	3.7 ± 0.3	3.1 ± 2.3	3.1 ± 22
27	1.3 ± 0.3	0.1 ± 1.5	0.1 ± 0.0	0.1 ± 0.0	1 ± 1	1.1 ± 0.1	0.5 ± 0.3	5.0 ± 3
EAIS	104.5 ± 3.9	2.8 ± 22.6	-1.9 ± 0.3	5.5 ± 0.0	90 ± 21	25.5 ± 1.0	12.0 ± 3.0	105.6 ± 29
WAIS	-175.7 ± 1.9	-7.8 ± 10.5	6.4 ± 0.2	10.1 ± 0.0	-169 ± 10	-2.1 ± 0.9	6.3 ± 5.2	-76.1 ± 49
APIS	-39.4 ± 2.4	1.4 ± 4.7	0.8 ± 1.7	0.9 ± 2.2	-39 ± 5	3.8 ± 0.4	5.0 ± 3.0	-14.1 ± 28
AIS	-110.5 ± 5.0	-3.7 ± 25.4	5.4 ± 1.8	16.4 ± 2.2	-118 ± 24	27.1 ± 1.5	23.2 ± 6.9	15.4 ± 65

Table S2.

Volume and mass change of Greenland grounded ice by drainage basin including Firn Air Content (FAC), Elastic and Glacier Isostatic Adjustment (GIA) corrections

Basin	dV/dt (km^3/y)			dFAC/dt (km^3/y)			Elastic uplift (km^3/y)			GIA (km^3/y)			Grounded Ice (Gt/y)		
1.1	-9.9	±	0.8	-4.1	±	1.4	0.3	±	0.1	0.1	±	0	-6	±	1.3
1.2	-3.7	±	0.6	-2.3	±	1.0	0.1	±	0	0.1	±	0	-1	±	0.9
1.3	-2.1	±	0.5	-1.4	±	0.7	0.0	±	0	0.2	±	0	-1	±	0.7
1.4	-1.5	±	0.3	-0.5	±	0.3	0.0	±	0	0.1	±	0	-1	±	0.3
2.1	-0.8	±	1.1	-3.6	±	3.3	0.2	±	0.1	0.1	±	0	2	±	3.1
2.2	2.0	±	0.5	-0.5	±	0.8	0.0	±	0	0.0	±	0	2	±	0.8
3.1	1.5	±	0.8	0.7	±	3.2	0.2	±	0.1	0.0	±	0	1	±	3
3.2	-7.4	±	0.4	-0.1	±	1.5	0.1	±	0	0.0	±	0	-7	±	1.4
3.3	-17.8	±	0.6	-0.7	±	2.7	0.3	±	0.1	0.0	±	0	-16	±	2.5
4.1	-17.5	±	0.5	-3.9	±	2.4	0.3	±	0.1	0.0	±	0	-13	±	2.2
4.2	-16.0	±	0.5	-3.2	±	2.7	0.3	±	0.1	0.0	±	0	-12	±	2.5
4.3	-10.8	±	0.4	-1.9	±	1.6	0.2	±	0	0.0	±	0	-8	±	1.5
5	-26.3	±	0.5	16.2	±	2.4	0.5	±	0.1	0.0	±	0	-40	±	6.2
6.1	-10.2	±	0.5	-2.4	±	2.1	0.2	±	0	0.0	±	0	-7	±	1.9
6.2	-20.6	±	0.8	-4.3	±	5.4	0.6	±	0.1	-0.2	±	0	-15	±	4.9
7.1	-22.7	±	0.7	-2.7	±	3.0	0.4	±	0.1	-0.2	±	0	-19	±	2.8
7.2	-12.7	±	0.8	-1.5	±	3.5	0.5	±	0.1	-0.2	±	0	-11	±	3.2
8.1	-49.8	±	1.1	-6.0	±	4.0	0.9	±	0.1	-0.3	±	0	-41	±	3.7
8.2	-8.6	±	0.4	-1.0	±	1.3	0.1	±	0	0.0	±	0	-7	±	1.2
Total	-235.0	±	2.8	-23.0	±	11.3	5.4	±	0.3	-0.5	±	0.1	-200	±	12

References and Notes

1. A. Shepherd, E. R. Ivins, G. A, V. R. Barletta, M. J. Bentley, S. Bettadpur, K. H. Briggs, D. H. Bromwich, R. Forsberg, N. Galin, M. Horwath, S. Jacobs, I. Joughin, M. A. King, J. T. M. Lenaerts, J. Li, S. R. M. Ligtenberg, A. Luckman, S. B. Luthcke, M. McMillan, R. Meister, G. Milne, J. Mouginot, A. Muir, J. P. Nicolas, J. Paden, A. J. Payne, H. Pritchard, E. Rignot, H. Rott, L. S. Sørensen, T. A. Scambos, B. Scheuchl, E. J. O. Schrama, B. Smith, A. V. Sundal, J. H. van Angelen, W. J. van de Berg, M. R. van den Broeke, D. G. Vaughan, I. Velicogna, J. Wahr, P. L. Whitehouse, D. J. Wingham, D. Yi, D. Young, H. J. Zwally, A reconciled estimate of ice-sheet mass balance. *Science* **338**, 1183–1189 (2012). doi:10.1126/science.1228102 Medline

2. IMBIE team, Mass balance of the Antarctic Ice Sheet from 1992 to 2017. *Nature* **558**, 219–222 (2018). [doi:10.1038/s41586-018-0179-y](doi:10.1038/s41586-018-0179-y) Medline

3. J. L. Bamber, R. M. Westaway, B. Marzeion, B. Wouters, The land ice contribution to sea level during the satellite era. *Environ. Res. Lett.* **13**, 63008 (2018). [doi:10.1088/1748-9326/aac2f0](doi:10.1088/1748-9326/aac2f0)

4. D. I. Benn, T. Cowton, J. Todd, A. Luckman, Glacier calving in Greenland. *Curr. Clim. Change Rep.* **3**, 282–290 (2017). [doi:10.1007/s40641-017-0070-1](doi:10.1007/s40641-017-0070-1) Medline

5. M. A. Depoorter, J. L. Bamber, J. A. Griggs, J. T. M. Lenaerts, S. R. M. Ligtenberg, M. R. van den Broeke, G. Moholdt, Calving fluxes and basal melt rates of Antarctic ice shelves. *Nature* **502**, 89–92 (2013). doi:10.1038/nature12567 Medline

6. E. Rignot, S. Jacobs, J. Mouginot, B. Scheuchl, Ice-shelf melting around Antarctica. *Science* **341**, 266–270 (2013). doi:10.1126/science.1235798 Medline

7. J. T. M. Lenaerts, B. Medley, M. R. van den Broeke, B. Wouters, Observing and modeling ice sheet surface mass balance. *Rev. Geophys.* **57**, 376–420 (2019). [doi:10.1029/2018RG000622](doi:10.1029/2018RG000622) Medline

8. E. Rignot, J. Mouginot, B. Scheuchl, M. van den Broeke, M. J. van Wessem, M. Morlighem, Four decades of Antarctic Ice Sheet mass balance from 1979–2017. *Proc. Natl. Acad. Sci. U.S.A.* **116**, 1095–1103 (2019). doi:10.1073/pnas.1812883116 Medline

9. M. van den Broeke, J. Bamber, J. Ettema, E. Rignot, E. Schrama, W. J. van de Berg, E. van Meijgaard, I. Velicogna, B. Wouters, Partitioning recent Greenland mass loss. *Science* **326**, 984–986 (2009). doi:10.1126/science.1178176 Medline

10. I. Joughin, B. E. Smith, I. M. Howat, D. Floricioiu, A. B. Richard, M. Truffer, M. Fahnestock, Seasonal to decadal scale variations in the surface velocity of Jakobshavn Isbrae, Greenland: Observation and model-based analysis. *J. Geophys. Res. Earth Surf.* 10.1029/2011JF002110 (2012).

11. B. M. Csatho, A. F. Schenk, C. J. van der Veen, G. Babonis, K. Duncan, S. Rezvanbehbahani, M. R. van den Broeke, S. B. Simonsen, S. Nagarajan, J. H. van Angelen, Laser altimetry reveals complex pattern of Greenland Ice Sheet dynamics. *Proc. Natl. Acad. Sci. U.S.A.* **111**, 18478–18483 (2014). doi:10.1073/pnas.1411680112 Medline

12. I. M. Howat, B. E. Smith, I. Joughin, T. A. Scambos, Rates of southeast Greenland ice volume loss from combined ICESat and ASTER observations. *Geophys. Res. Lett.* **35**, L17505 (2008). [doi:10.1029/2008GL034496](doi:10.1029/2008GL034496)

13. N. Wilson, F. Straneo, P. Heimbach, Satellite-derived submarine melt rates and mass balance (2011–2015) for Greenland's largest remaining ice tongues. *Cryosphere* **11**, 2773–2782 (2017). [doi:10.5194/tc-11-2773-2017](doi:10.5194/tc-11-2773-2017)

14. M. Thoma, A. Jenkins, D. Holland, S. Jacobs, Modelling Circumpolar Deep Water intrusions on the Amundsen Sea continental shelf, Antarctica. *Geophys. Res. Lett.* **35**, L18602 (2008). [doi:10.1029/2008GL034939](doi:10.1029/2008GL034939)

15. H. D. Pritchard, S. R. M. Ligtenberg, H. A. Fricker, D. G. Vaughan, M. R. van den Broeke, L. Padman, Antarctic ice-sheet loss driven by basal melting of ice shelves. *Nature* **484**, 502–505 (2012). doi:10.1038/nature10968 Medline

16. F. S. Paolo, H. A. Fricker, L. Padman, Ice sheets. Volume loss from Antarctic ice shelves is accelerating. *Science* **348**, 327–331 (2015). doi:10.1126/science.aaa0940 Medline

17. J. J. Fürst, G. Durand, F. Gillet-Chaulet, L. Tavard, M. Rankl, M. Braun, O. Gagliardini, The safety band of Antarctic ice shelves. *Nat. Clim. Chang.* **6**, 479–482 (2016). doi:10.1038/nclimate2912

18. T. K. Dupont, R. B. B. Alley, Assessment of the importance of ice-shelf buttressing to ice-sheet flow. *Geophys. Res. Lett.* **32**, 1–4 (2005). [doi:10.1029/2004GL022024](doi:10.1029/2004GL022024)

19. T. A. Scambos, J. A. Bohlander, C. A. Shuman, P. Skvarca, Glacier acceleration and thinning after ice shelf collapse in the Larsen B embayment, Antarctica. *Geophys. Res. Lett.* **31**, L18402 (2004). [doi:10.1029/2004GL020670](doi:10.1029/2004GL020670)

20. E. Rignot, J. Mouginot, M. Morlighem, H. Seroussi, B. Scheuchl, Widespread, rapid grounding line retreat of Pine Island, Thwaites, Smith, and Kohler glaciers, West Antarctica, from 1992 to 2011. *Geophys. Res. Lett.* **41**, 3502–3509 (2014). [doi:10.1002/2014GL060140](doi:10.1002/2014GL060140)

21. D. J. Wingham, A. Shepherd, A. Muir, G. J. Marshall, Mass balance of the Antarctic ice sheet. *Philos. Trans. A Math. Phys. Eng. Sci.* **364**, 1627–1635 (2006). doi:10.1098/rsta.2006.1792 Medline

22. H. J. Zwally, M. B. Giovinetto, J. Li, H. G. Cornejo, M. A. Beckley, A. C. Brenner, J. L. Saba, D. Yi, Mass changes of the Greenland and Antarctic ice sheets and shelves and contributions to sea-level rise: 1992–2002. *J. Glaciol.* **51**, 509–527 (2005). [doi:10.3189/172756505781829007](doi:10.3189/172756505781829007)

23. H. D. Pritchard, R. J. Arthern, D. G. Vaughan, L. A. Edwards, Extensive dynamic thinning on the margins of the Greenland and Antarctic ice sheets. *Nature* **461**, 971–975 (2009). doi:10.1038/nature08471 Medline

24. A. A. Borsa, H. A. Fricker, K. M. Brunt, A Terrestrial Validation of ICESat Elevation Measurements and Implications for Global Reanalyses. *IEEE Trans. Geosci. Remote Sens.* **57**, 6946–6959 (2019). doi:10.1109/TGRS.2019.2909739

25. Materials and methods are available as supplementary materials.

26. J. C. Ryan, A. Hubbard, M. Stibal, T. D. Irvine-Fynn, J. Cook, L. C. Smith, K. Cameron, J. Box, Dark zone of the Greenland Ice Sheet controlled by distributed biologically-active impurities. *Nat. Commun.* **9**, 1065 (2018). doi:10.1038/s41467-018-03353-2 Medline

27. M. R. van den Broeke, E. M. Enderlin, I. M. Howat, P. Kuipers Munneke, B. P. Y. Noël, W. J. van de Berg, E. van Meijgaard, B. Wouters, On the recent contribution of the Greenland ice sheet to sea level change. *Cryosphere* **10**, 1933–1946 (2016). doi:10.5194/tc-10-1933-2016

28. X. Fettweis, J. E. Box, C. Agosta, C. Amory, C. Kittel, C. Lang, D. Van As, H. Machguth, H. Gallée, Reconstructions of the 1900-2015 Greenland ice sheet surface mass balance using the regional climate MAR model. *Cryosphere* **11**, 1015–1033 (2017). doi:10.5194/tc-11-1015-2017

29. M. Wood, E. Rignot, I. Fenty, D. Menemenlis, R. Millan, M. Morlighem, J. Mouginot, H. Seroussi, Ocean-induced melt triggers glacier retreat in Northwest Greenland. *Geophys. Res. Lett.* **45**, 8334–8342 (2018). doi:10.1029/2018GL078024

30. D. Slater, F. Straneo, D. Felikson, C. Little, H. Goelzer, X. Fettweis, J. Holte, Estimating Greenland tidewater glacier retreat driven by submarine melting. *Cryosphere* **13**, 2489–2509 (2019). doi:10.5194/tc-13-2489-2019

31. T. Moon, I. Joughin, B. Smith, Seasonal to multiyear variability of glacier surface velocity, terminus position, and sea ice/ice mélange in northwest Greenland. *J. Geophys. Res. Earth Surf.* **120**, 818–833 (2015). doi:10.1002/2015JF003494

32. E. Rignot, P. Kanagaratnam, Changes in the velocity structure of the Greenland Ice Sheet. *Science* **311**, 986–990 (2006). doi:10.1126/science.1121381 Medline

33. S. A. Khan, K. H. Kjær, M. Bevis, J. L. Bamber, J. Wahr, K. K. Kjeldsen, A. A. Bjørk, N. J. Korsgaard, L. A. Stearns, M. R. van den Broeke, L. Liu, N. K. Larsen, I. S. Muresan, Sustained mass loss of the northeast Greenland ice sheet triggered by regional warming. *Nat. Clim. Chang.* **4**, 292–299 (2014). doi:10.1038/nclimate2161

34. I. Joughin, B. E. Smith, D. E. Shean, D. Floricioiu, Brief communication: Further summer speedup of Jakobshavn Isbræ. *Cryosphere* **8**, 209–214 (2014). doi:10.5194/tc-8-209-2014

35. I. Joughin, W. Abdalati, M. Fahnestock, Large fluctuations in speed on Greenland's Jakobshavn Isbrae glacier. *Nature* **432**, 608–610 (2004). doi:10.1038/nature03130 Medline

36. A. Khazendar, I. G. Fenty, D. Carroll, A. Gardner, C. M. Lee, I. Fukumori, O. Wang, H. Zhang, H. Seroussi, D. Moller, B. P. Y. Noël, M. R. van den Broeke, S. Dinardo, J. Willis, Interruption of two decades of Jakobshavn Isbrae acceleration and thinning as regional ocean cools. *Nat. Geosci.* **12**, 277–283 (2019). doi:10.1038/s41561-019-0329-3

37. M. Morlighem, E. Rignot, T. Binder, D. Blankenship, R. Drews, G. Eagles, O. Eisen, F. Ferraccioli, R. Forsberg, P. Fretwell, V. Goel, J. S. Greenbaum, H. Gudmundsson, J. Guo, V. Helm, C. Hofstede, I. Howat, A. Humbert, W. Jokat, N. B. Karlsson, W. S. Lee, K. Matsuoka, R. Millan, J. Mouginot, J. Paden, F. Pattyn, J. Roberts, S. Rosier, A. Ruppel, H. Seroussi, E. C. Smith, D. Steinhage, B. Sun, M. R. van den Broeke, T. D. van Ommen, M. van Wessem, D. A. Young, Deep glacial troughs and stabilizing ridges

unveiled beneath the margins of the Antarctic ice sheet. *Nat. Geosci.* **13**, 132–137 (2020). [doi:10.1038/s41561-019-0510-8](doi:10.1038/s41561-019-0510-8)

38. G. A. Catania, T. A. Scambos, H. Conway, C. F. Raymond, Sequential stagnation of Kamb Ice Stream, West Antarctica. *Geophys. Res. Lett.* **33**, L14502 (2006). [doi:10.1029/2006GL026430](doi:10.1029/2006GL026430)

39. L. H. Beem, S. M. Tulaczyk, M. A. King, M. Bougamont, H. A. Fricker, P. Christoffersen, Variable deceleration of Whillans Ice Stream, West Antarctica. *J. Geophys. Res. Earth Surf.* **119**, 212–224 (2014). [doi:10.1002/2013JF002958](doi:10.1002/2013JF002958)

40. IMBIE Team, Mass balance of the Greenland Ice Sheet from 1992 to 2018. *Nature* **579**, 233–239 (2020). [doi:10.1038/s41586-019-1855-2](doi:10.1038/s41586-019-1855-2) Medline

41. J. Mouginot, E. Rignot, A. A. Bjørk, M. van den Broeke, R. Millan, M. Morlighem, B. Noël, B. Scheuchl, M. Wood, Forty-six years of Greenland Ice Sheet mass balance from 1972 to 2018. *Proc. Natl. Acad. Sci. U.S.A.* **116**, 9239–9244 (2019). doi:10.1073/pnas.1904242116 Medline

42. M. D. King, I. M. Howat, S. Jeong, M. J. Noh, B. Wouters, B. Noël, M. R. van den Broeke, Seasonal to decadal variability in ice discharge from the Greenland Ice Sheet. *Cryosphere* **12**, 3813–3825 (2018). [doi:10.5194/tc-12-3813-2018](doi:10.5194/tc-12-3813-2018) Medline

43. G. H. Gudmundsson, F. S. Paolo, S. Adusumilli, H. A. Fricker, Instantaneous Antarctic ice sheet mass loss driven by thinning ice shelves. *Geophys. Res. Lett.* **46**, 13903–13909 (2019). [doi:10.1029/2019GL085027](doi:10.1029/2019GL085027)

44. K. J. Tinto, L. Padman, C. S. Siddoway, S. R. Springer, H. A. Fricker, I. Das, F. Caratori Tontini, D. F. Porter, N. P. Frearson, S. L. Howard, M. R. Siegfried, C. Mosbeux, M. K. Becker, C. Bertinato, A. Boghosian, N. Brady, B. L. Burton, W. Chu, S. I. Cordero, T. Dhakal, L. Dong, C. D. Gustafson, S. Keeshin, C. Locke, A. Lockett, G. O'Brien, J. J. Spergel, S. E. Starke, M. Tankersley, M. G. Wearing, R. E. Bell, Ross Ice Shelf response to climate driven by the tectonic imprint on seafloor bathymetry. *Nat. Geosci.* **12**, 441–449 (2019). [doi:10.1038/s41561-019-0370-2](doi:10.1038/s41561-019-0370-2)

45. X. Sun, J. B. Abshire, A. A. Borsa, H. A. Fricker, D. Yi, J. P. DiMarzio, F. S. Paolo, K. M. Brunt, D. J. Harding, G. A. Neumann, ICESat/GLAS Altimetry Measurements: Received Signal Dynamic Range and Saturation Correction. *IEEE Trans. Geosci. Remote Sens.* **55**, 5440–5454 (2017). doi:10.1109/TGRS.2017.2702126 Medline

46. B. E. Schutz, H. J. Zwally, C. A. Shuman, D. Hancock, J. P. DiMarzio, Overview of the ICESat mission. *Geophys. Res. Lett.* **32**, L21S01 (2005). [doi:10.1029/2005GL024009](doi:10.1029/2005GL024009)

47. J. B. Abshire, X. Sun, H. Riris, J. M. Sirota, J. F. McGarry, S. Palm, D. Yi, P. Liiva, Geoscience Laser Altimeter System (GLAS) on the ICESat mission: On-orbit measurement performance. *Geophys. Res. Lett.* **32**, L21S02 (2005). [doi:10.1029/2005GL024028](doi:10.1029/2005GL024028)

48. T. Markus, T. Neumann, A. Martino, W. Abdalati, K. Brunt, B. Csatho, S. Farrell, H. Fricker, A. Gardner, D. Harding, M. Jasinski, R. Kwok, L. Magruder, D. Lubin, S. Luthcke, J. Morison, R. Nelson, A. Neuenschwander, S. Palm, S. Popescu, C. K. Shum, B. E. Schutz, B. Smith, Y. Yang, J. Zwally, The Ice, Cloud, and land Elevation Satellite-2

(ICESat-2): Science requirements, concept, and implementation. *Remote Sens. Environ.* **190**, 260–273 (2017). doi:10.1016/j.rse.2016.12.029

49. D. Felikson, T. C. Bartholomaus, G. A. Catania, N. J. Korsgaard, K. H. Kjær, M. Morlighem, B. Noël, M. van den Broeke, L. A. Stearns, E. L. Shroyer, D. A. Sutherland, J. D. Nash, Inland thinning on the Greenland ice sheet controlled by outlet glacier geometry. *Nat. Geosci.* **10**, 366–369 (2017). doi:10.1038/ngeo2934

50. T. A. Neumann, A. J. Martino, T. Markus, S. Bae, M. R. Bock, A. C. Brenner, K. M. Brunt, J. Cavanaugh, S. T. Fernandes, D. W. Hancock, K. Harbeck, J. Lee, N. T. Kurtz, P. J. Luers, S. B. Luthcke, L. Magruder, T. A. Pennington, L. Ramos-Izquierdo, T. Rebold, J. Skoog, T. C. Thomas, The Ice, Cloud, and Land Elevation Satellite–2 Mission: A global geolocated photon product derived from the advanced topographic laser altimeter system. *Remote Sens. Environ.* **233**, 111325 (2019). doi:10.1016/j.rse.2019.111325 Medline

51. B. Smith, H. A. Fricker, N. Holschuh, A. S. Gardner, S. Adusumilli, K. M. Brunt, B. Csatho, K. Harbeck, A. Huth, T. Neumann, J. Nilsson, M. R. Siegfried, Land ice height-retrieval algorithm for NASA's ICESat-2 photon-counting laser altimeter. *Remote Sens. Environ.* **233**, 111352 (2019). doi:10.1016/j.rse.2019.111352

52. R. Kwok, G. F. Cunningham, J. Hoffmann, T. Markus, Testing the ice-water discrimination and freeboard retrieval algorithms for the ICESat-2 mission. *Remote Sens. Environ.* **183**, 13–25 (2016). doi:10.1016/j.rse.2016.05.011

53. A. Neuenschwander, K. Pitts, The ATL08 land and vegetation product for the ICESat-2 Mission. *Remote Sens. Environ.* **221**, 247–259 (2019). doi:10.1016/j.rse.2018.11.005

54. S. C. Popescu, T. Zhou, R. Nelson, A. Neuenschwander, R. Sheridan, L. Narine, K. M. Walsh, Photon counting LiDAR: An adaptive ground and canopy height retrieval algorithm for ICESat-2 data. *Remote Sens. Environ.* **208**, 154–170 (2018). doi:10.1016/j.rse.2018.02.019

55. H. J. Zwally, R. Schutz, C. Bentley, J. Bufton, T. Herring, J. Minster, J. Spinhirne, R. Thomas, *GLAS/ICESat L2 Antarctic and Greenland Ice Sheet Altimetry Data*, version 34 (National Snow and Ice Data Center, 2014); http://doi.org/10.5067/ICESAT/GLAS/DATA225

56. A. A. Borsa, G. Moholdt, H. A. Fricker, K. M. Brunt, A range correction for ICESat and its potential impact on ice-sheet mass balance studies. *Cryosphere* **8**, 345–357 (2014). doi:10.5194/tc-8-345-2014

57. L. Padman, H. A. Fricker, R. Coleman, S. Howard, L. Erofeeva, A new tide model for the Antarctic ice shelves and seas. *Ann. Glaciol.* **34**, 247–254 (2002). doi:10.3189/172756402781817752

58. G. D. Egbert, A. F. Bennett, M. G. G. Foreman, TOPEX/POSEIDON tides estimated using a global inverse model. *J. Geophys. Res. Atmos.* **99**, 821–852 (1994). doi:10.1029/94JC01894

59. G. D. Egbert, S. Y. Erofeeva, Efficient inverse modeling of barotropic ocean tides. *J. Atmos. Ocean. Technol.* **19**, 183–204 (2002). doi:10.1175/1520-0426(2002)019<0183:EIMOBO>2.0.CO;2

60. B. Smith, H. A. Fricker, A. Gardner, M. R. Siegfried, S. Adusumilli, B. M. Csathó, N. Holschuh, J. Nilsson, F. S. Paolo, The ICESat-2 Science Team, ATLAS/ICESat-2 L3A Land Ice Height, version 1 (National Snow and Ice Data Center, 2019); 10.5067/ATLAS/ATL06.001

61. H. J. Zwally, J. Li, J. W. Robbins, J. L. Saba, D. Yi, A. C. Brenner, Mass gains of the Antarctic Ice Sheet exceed losses. *J. Glaciol.* **61**, 1019–1036 (2015). doi:10.3189/2015JoG15J071

62. C. H. Davis, A. C. Ferguson, Elevation change of the Sntarctic Ice Sheet, 1995–2000, from ERS-2 satellite radar altimetry. *IEEE Trans. Geosci. Remote Sens.* **42**, 2437–2445 (2004). doi:10.1109/TGRS.2004.836789

63. F. S. Paolo, H. A. Fricker, L. Padman, Constructing improved decadal records of Antarctic ice shelf height change from multiple satellite radar altimeters. *Remote Sens. Environ.* **177**, 192–205 (2016). doi:10.1016/j.rse.2016.01.026

64. S. R. M. Ligtenberg, M. M. Helsen, M. R. van den Broeke, An improved semi-empirical model for the densification of Antarctic firn. *Cryosphere* **5**, 809–819 (2011). doi:10.5194/tc-5-809-2011

65. P. Kuipers Munneke, S. R. M. Ligtenberg, B. P. Y. Noël, I. M. Howat, J. E. Box, E. Mosley-Thompson, J. R. McConnell, K. Steffen, J. T. Harper, S. B. Das, M. R. van den Broeke, Elevation change of the Greenland Ice Sheet due to surface mass balance and firn processes, 1960-2013. *Cryosphere Discuss.* **9**, 3541–3580 (2015). doi:10.5194/tcd-9-3541-2015

66. C. M. Stevens, thesis, University of Washington (2018).

67. J. M. D. Lundin, C. M. Stevens, R. Arthern, C. Buizert, A. Orsi, S. R. M. Ligtenberg, S. B. Simonsen, E. Cummings, R. Essery, W. Leahy, P. Harris, M. M. Helsen, E. D. Waddington, Firn Model Intercomparison Experiment (FirnMICE). *J. Glaciol.* **63**, 401–422 (2017). doi:10.1017/jog.2016.114

68. M. M. Herron, C. C. Langway, Firn densification: An empirical model. *J. Glaciol.* **25**, 373–385 (1980). doi:10.1017/S0022143000015239

69. J. Li, H. J. Zwally, Modeling the density variation in the shallow firn layer. *Ann. Glaciol.* **38**, 309–313 (2004). doi:10.3189/172756404781814988

70. J. Li, H. J. Zwally, Response times of ice-sheet surface heights to changes in the rate of Antarctic firn compaction caused by accumulation and temperature variations. *J. Glaciol.* **61**, 1037–1047 (2015). doi:10.3189/2015JoG14J182

71. R. J. Arthern, D. G. Vaughan, A. M. Rankin, R. Mulvaney, E. R. Thomas, In situ measurements of Antarctic snow compaction compared with predictions of models. *J. Geophys. Res. Earth Surf.* **115**, 1–12 (2010).

72. V. Verjans, A. A. Leeson, C. M. Stevens, M. MacFerrin, B. Noël, M. R. van den Broeke, Development of physically based liquid water schemes for Greenland firn-densification models. *Cryosphere* **13**, 1819–1842 (2019). doi:10.5194/tc-13-1819-2019

73. R. Gelaro, W. McCarty, M. J. Suárez, R. Todling, A. Molod, L. Takacs, C. Randles, A. Darmenov, M. G. Bosilovich, R. Reichle, K. Wargan, L. Coy, R. Cullather, C. Draper, S.

Akella, V. Buchard, A. Conaty, A. da Silva, W. Gu, G. K. Kim, R. Koster, R. Lucchesi, D. Merkova, J. E. Nielsen, G. Partyka, S. Pawson, W. Putman, M. Rienecker, S. D. Schubert, M. Sienkiewicz, B. Zhao, The modern-era retrospective analysis for research and applications, version 2 (MERRA-2). *J. Clim.* **30**, 5419–5454 (2017). doi:10.1175/JCLI-D-16-0758.1 Medline

74. B. Medley, E. R. Thomas, Increased snowfall over the Antarctic Ice Sheet mitigated twentieth-century sea-level rise. *Nat. Clim. Chang.* **9**, 34–39 (2019). doi:10.1038/s41558-018-0356-x

75. B. Huai, Y. Wang, M. Ding, J. Zhang, X. Dong, An assessment of recent global atmospheric reanalyses for Antarctic near surface air temperature. *Atmos. Res.* **226**, 181–191 (2019). doi:10.1016/j.atmosres.2019.04.029

76. B. Noël, W. J. van de Berg, J. M. van Wessem, E. van Meijgaard, D. van As, J. T. M. Lenaerts, S. Lhermitte, P. Kuipers Munneke, C. J. P. P. Smeets, L. H. van Ulft, R. S. W. van de Wal, M. R. van den Broeke, Modelling the climate and surface mass balance of polar ice sheets using RACMO2 - Part 1: Greenland (1958-2016). *Cryosphere* **12**, 811–831 (2018). doi:10.5194/tc-12-811-2018

77. J. M. van Wessem, W. J. van de Berg, B. P. Y. Noël, E. van Meijgaard, C. Amory, G. Birnbaum, C. L. Jakobs, K. Krüger, J. T. M. Lenaerts, S. Lhermitte, S. R. M. Ligtenberg, B. Medley, C. H. Reijmer, K. van Tricht, L. D. Trusel, L. H. van Ulft, B. Wouters, J. Wuite, M. R. van den Broeke, Modelling the climate and surface mass balance of polar ice sheets using RACMO2, part 2: Antarctica (1979-2016). *Cryosphere* **12**, 1479–1498 (2018). doi:10.5194/tc-12-1479-2018

78. C. Agosta, C. Amory, C. Kittel, A. Orsi, V. Favier, H. Gallée, M. R. van den Broeke, J. T. M. Lenaerts, J. M. van Wessem, X. Fettweis, Estimation of the Antarctic surface mass balance using MAR (1979–2015) and identification of dominant processes. *Cryosphere Discuss.* **13**, 1–22 (2018).

79. M. van den Broeke, C. Bus, J. Ettema, P. Smeets, Temperature thresholds for degree-day modelling of Greenland ice sheet melt rates. *Geophys. Res. Lett.* **37**, 1–5 (2010). doi:10.1029/2010GL044123

80. L. D. Trusel, K. E. Frey, S. B. Das, P. K. Munneke, M. R. van den Broeke, Satellite-based estimates of Antarctic surface meltwater fluxes. *Geophys. Res. Lett.* **40**, 6148–6153 (2013). doi:10.1002/2013GL058138

81. H. Zwally, Jay, Mario B. Giovinetto, Matthew A. Beckley, and Jack L. Saba, 2012, Antarctic and Greenland Drainage Systems, GSFC Cryospheric Sciences Laboratory; http://icesat4.gsfc.nasa.gov/cryo_data/ant_grn_drainage_systems.php.

82. P. Kuipers Munneke, S. R. M. Ligtenberg, B. P. Y. Noël, I. M. Howat, J. E. Box, E. Mosley-Thompson, J. R. McConnell, K. Steffen, J. T. Harper, S. B. Das, M. R. van den Broeke, Elevation change of the Greenland Ice Sheet due to surface mass balance and firn processes, 1960–2014. *Cryosphere* **9**, 2009–2025 (2015). doi:10.5194/tc-9-2009-2015

83. A. S. Gardner, G. Moholdt, T. Scambos, M. Fahnstock, S. Ligtenberg, M. van den Broeke, J. Nilsson, Increased West Antarctic and unchanged East Antarctic ice discharge over the last 7 years. *Cryosphere* **12**, 521–547 (2018). doi:10.5194/tc-12-521-2018

84. J. Fyke, J. T. M. Lenaerts, H. Wang, Basin-scale heterogeneity in Antarctic precipitation and its impact on surface mass variability. *Cryosphere* **11**, 2595–2609 (2017). doi:10.5194/tc-11-2595-2017

85. E. R. Ivins, T. S. James, J. Wahr, E. J. O. Schrama, F. W. Landerer, K. M. Simon, Antarctic contribution to sea level rise observed by GRACE with improved GIA correction. *J. Geophys. Res. Solid Earth* **118**, 3126–3141 (2013). doi:10.1002/jgrb.50208

86. P. L. Whitehouse, M. J. Bentley, G. A. Milne, M. A. King, I. D. Thomas, A new glacial isostatic adjustment model for Antarctica: Calibrated and tested using observations of relative sea-level change and present-day uplift rates. *Geophys. J. Int.* **190**, 1464–1482 (2012). doi:10.1111/j.1365-246X.2012.05557.x

87. K. G. Miller, J. D. Wright, J. V. Browning, A. Kulpecz, M. Kominz, T. R. Naish, B. S. Cramer, Y. Rosenthal, W. R. Peltier, S. Sosdian, High tide of the warm pliocene: Implications of global sea level for Antarctic deglaciation. *Geology* **40**, 407–410 (2012). doi:10.1130/G32869.1

88. W. Richard Peltier, D. F. Argus, R. Drummond, Comment on "An Assessment of the ICE-6G_C (VM5a) Glacial Isostatic Adjustment Model" by Purcell et al. *J. Geophys. Res. Solid Earth* **123**, 2019–2028 (2018). doi:10.1002/2016JB013844

89. M. J. R. Simpson, G. A. Milne, P. Huybrechts, A. J. Long, Calibrating a glaciological model of the Greenland ice sheet from the Last Glacial Maximum to present-day using field observations of relative sea level and ice extent. *Quat. Sci. Rev.* **28**, 1631–1657 (2009). doi:10.1016/j.quascirev.2009.03.004

90. J. Wahr, D. Wingham, C. Bentley, A method of combining ICESat and GRACE satellite data to constrain Antarctic mass balance. *J. Geophys. Res. Solid Earth* **105** (B7), 16279–16294 (2000). doi:10.1029/2000JB900113

91. W. E. Farrell, Deformation of the Earth by surface loads. *Rev. Geophys.* **10**, 761–797 (1972). doi:10.1029/RG010i003p00761

92. H. R. Martens, L. Rivera, M. Simons, LoadDef: A Python-based toolkit to model elastic deformation caused by surface mass loading on spherically symmetric bodies. *Earth Space Sci.* **6**, 311–323 (2019). doi:10.1029/2018EA000462 Medline

93. A. M. Dziewonski, D. L. Anderson, Preliminary reference Earth model. *Phys. Earth Planet. Inter.* **25**, 297–356 (1981). doi:10.1016/0031-9201(81)90046-7

94. M. A. Lazzara, K. C. Jezek, T. A. Scambos, D. R. MacAyeal, C. J. Van Der Veen, On the recent calving of icebergs from the Ross ice shelf. *Polar Geogr.* **31**, 15–26 (1999). doi:10.1080/10889370802175937

95. H. A. Fricker, N. W. Young, I. Allison, R. Coleman, Iceberg calving from the Amery Ice Shelf, East Antarctica. *Ann. Glaciol.* **34**, 241–246 (2002). doi:10.3189/172756402781817581

96. J. Mouginot, B. Scheuchl, E. Rignot, MEaSUREs Antarctic Boundaries for IPY 2007-2009 from Satellite Radar, version 2, (National Snow and Ice Data Center, 2017); 10.5067/AXE4121732AD

97. A. E. Hogg, G. H. Gudmundsson, Impacts of the Larsen-C Ice Shelf calving event. *Nat. Clim. Chang.* **7**, 540–542 (2017). doi:10.1038/nclimate3359

98. K. M. Brunt, T. A. Neumann, C. F. Larsen, Assessment of altimetry using ground-based GPS data from the 88S Traverse, Antarctica, in support of ICESat-2. *Cryosphere* **13**, 579–590 (2019). doi:10.5194/tc-13-579-2019

99. K. M. Brunt, T. A. Neumann, B. E. Smith, First assessment of ICESat-2 Ice-Sheet surface heights, based on comparisons over the interior of the Antarctic ice sheet. *Geophys. Res. Lett.* 10.1029/2019GL084886 (2019).

100. J. F. Zumberge, M. B. Heflin, D. C. Jefferson, M. M. Watkins, F. H. Webb, Precise point positioning for the efficient and robust analysis of GPS data from large networks. *J. Geophys. Res. Solid Earth* **102**, 5005–5017 (1997). doi:10.1029/96JB03860